LASER
& PHOTONICS
REVIEWS

Supporting Information

for *Laser Photonics Rev.*, DOI 10.1002/lpor.202301148

Tip-Enhanced Imaging and Control of Infrared Strong Light-Matter Interaction

Yueying Wang, Samuel C. Johnson, Nishant Nookala, John F. Klem, Samuel R. Turner, Richard L. Puro, Min Hu, Igal Brener, Eric A. Muller, Alexey Belyanin*, Mikhail A. Belkin* and Markus B. Raschke**

Supplementary information for Tip-enhanced imaging and control of infrared strong light-matter interaction

Yueying Wang,[1,2,*] Samuel C. Johnson,[1,*] Nishant Nookala,[3] John F. Klem,[4] Samuel R. Turner,[1,5] Richard L. Puro,[1] Min Hu,[2] Igal Brener,[4] Eric A. Muller,[6,†] Alexey Belyanin,[7,‡] Mikhail A. Belkin,[8,§] and Markus B. Raschke[1,¶]

[1]*Department of Physics and JILA, University of Colorado, Boulder, CO, 80309, USA*

[2]*Terahertz Research Center, School of Electronic Science and Engineering, University of Electronic Science and Technology of China, Chengdu, 610054, China*

[3]*Department of Electrical and Computer Engineering, The University of Texas at Austin, Austin, Texas 78712, USA*

[4]*Sandia National Laboratories, Albuquerque, New Mexico 87185, USA*

[5]*Advanced Light Source, Lawrence Berkeley National Laboratory, Berkeley, California 94720, United States*

[6]*Department of Chemistry, Colgate University, 13 Oak Drive, Hamilton, New York 13346, United States*

[7]*Department of Physics and Astronomy, Texas A&M University, College Station 77843, Texas, United States*

[8]*Walter Schottky Institute, Technical University of Munich, 85748 Garching, Germany*

(Dated: June 20, 2024)

S1 METHODS

S1.1 Sample fabrication

The epilayer of the grown wafer was coated with Ti, Pt, and Au layers of 10, 20, and 200 nm, respectively, and the wafer was then thermocompressively bonded upside-down to a host InP substrate. The original substrate was then removed via mechanical polishing and selective wet chemical etching, exposing the epilayer on a metal ground plane. The top metal layer of the future nano-antennas made of 10 nm of Ti and 100 nm of Au was then evaporated and a 300-nm-thick $\mathrm{Si_xN_y}$ hard mask was deposited on top of the metal. The dipole resonators were then defined via electron-beam lithography and successive dry etching steps. Finally, the hard mask was removed to produce the structures shown in Fig. 1b. Intersubband absorption measurements of the MQW structure indicate a nominal transition frequency between the ground state and the first excited electronic state of $\tilde{\nu}_{21} \simeq 1260\ \mathrm{cm}^{-1}$, in good agreement with simulations [1].

S1.2 Antenna modes

The Fig. S1a shows the spectrum of an array of antennas coupled to MQW across a large frequency range of 700 to 4000 cm. The MQW transition is apparent at 1310 cm^{-1}, with the antenna dipole mode at 1865 cm^{-1}, and the quadrupole mode at 3100 cm^{-1}as the first higher order multipole resonances of the antenna.

We note that in Fig. 2a, the antenna linewidth is seen to increase slightly from 100 cm^{-1} for antennas with the lowest resonance to 140 cm^{-1} for antennas with the highest response. Although the linewidth increases slightly, it also represents a slight increase in Q-factor for higher wavenumber antennas. This modest linewidth change is expected for half-wavelength dipole antennas across the full octave of tuning.

S1.3 Radiative and non-radiative decay of ISB transition

Non-radiative rates for ISB transitions in our case are estimated to be at least three orders of magnitude higher than radiative rates. Non-radiative relaxation rates between electron subbands separated by energies higher than energies of optical phonons in a semiconductor system (which is the case of our MQW stack) are known to be $\sim$ 1/ps [2]. In comparison, the radiative recombina-

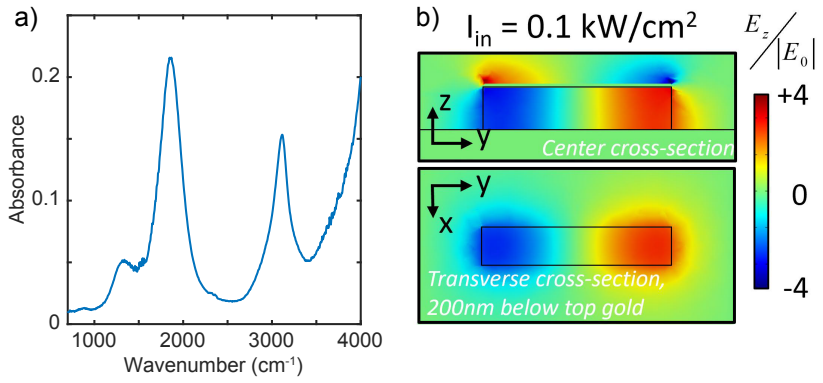

Figure S1. (a) Broadband antenna-MQW absorption spectra with MQW transition at 1310 cm^{-1}, the antenna dipole resonance at 1865 cm^{-1} and the quadrupole mode at 3100 cm^{-1}. (b) Simulation of the IR near-field distribution of the antenna-MQW structure.

tion rate of an optical transition with an energy of 100 - 200 meV and a transition dipole moment of 1 nm $\times e$ (e is the electron charge) is $\sim$ 1/10 ns, see [3] for a typical analysis.

Due to the deep subwavelength MQW stack thickness of 400 nm, the electric field at the pump frequencies has a nearly uniform field distribution across the layers. Fig. S1b shows the field contribution of a typical antenna dipole field.

The dipole field distribution across the antenna itself, however, is not expected to lead to a broadening of the linewidth of the MQW transition, at least at lower field intensities, as in our experiment. The transition energy itself corresponding to the MQW band structure, does not depend on the optical field strength. Built-in electric fields due to Schottky contact at the metal-semiconductor interface may lead to some inhomogeneous broadening of intersubband transitions in the MQW. This effect, however, would be too small to be discernible in the optical spectra of the antenna-MQW system.

S1.4 IR s-SNOM measurements

For IR s-SNOM measurements, we focus the incident light on the atomic force microscopy (AFM) nanotip. We use the commercial metallic AFM tips (Pt/Ir coated, ARROW-NCPt-50, NANO World, tapping at frequency 250 kHz), with the tapping amplitude 100 nm. The scattered signal is collected in a back-scattering geometry by the off-axis parabolic mirror (OAP, focal length=11 mm, NA 0.46), then detected by the liquid nitrogen cooled Mercury Cadmium Telluride

(MCT, KV104-0.5-A-1-SMA, KOLMAR Technologies) detector with 2-11 μm wavelength range, and finally demodulated by the integrated lock-in amplifier.

For the nano-FTIR detection, the interferometric detection in a Michelson geometry can provide the optical homodyne amplification of the near-field signal, and also the suppression of the background scattering, which is treated as noise. The spectrum is collected at $16\mathrm{cm}^{-1}$spectral resolution, with 10 times averaging.

For the pseudo-heterodyne detection, the reference arm is phase-modulated by a vibrating mirror at 307 Hz. The sideband demodulation can provide sufficient background suppression, resulting in clear near-field phase ϕ_{NF} and amplitude A_{NF} information with nano-scale resolution. The phase nano-images ϕ_{NF} are collected with 100×100 pixels, with 40 ms integration time per pixel. To average the phase data along the antenna at different frequencies, we average the data points at the center of the antenna, then subtract the value over the whole antenna, as the background.

S2 MODEL

S2.1 Two-oscillator model

We set up a two-oscillator model to study the optical interaction between antenna and quantum well, which are treated as the simple harmonic oscillators, with mutual linear coupling terms. The transitions of the MQW and the electronic response of the antenna can be described by a change in charge displacement x_{qw} and x_{ant}, spring constants k_{ant} and k_{qw}, Lorentzian damping γ_{qw} and γ_{ant} , and coupling between antenna and quantum well κ_{aq}. Including the optical driving field $\frac{e}{m}E_{ant}(t)$, the equations of motion for the quantum well and antenna become:

$$\ddot{x}_{ant} + \gamma_{ant}\dot{x}_{ant} + k_{ant}x_{ant} + \kappa_{aq}(x_{ant} - x_{qw}) = \frac{e}{m}E_{ant}(t) \tag{S.1}$$

$$\ddot{x}_{qw} + \gamma_{qw}\dot{x}_{qw} + k_{qw}x_{qw} + \kappa_{aq}(x_{qw} - x_{ant}) = 0 \tag{S.2}$$

We then solve the steady state solutions of the coupled system. In the limit of low damping, find the resonance frequencies of the hybridized modes, $\omega_{\pm}$.

$$\omega_{\pm}^2 = \frac{1}{2}\left[\omega_{ant}^2 + \omega_{qw}^2 \pm \sqrt{(\omega_{ant}^2 - \omega_{qw}^2)^2 + 4g_{aq}^2\omega_{ant}\omega_{qw}}\right]. \tag{S.3}$$

where $\omega_{ant} = \sqrt{k_{ant} + \kappa_{aq}}$, $\omega_{ant} = \sqrt{k_{ant} + \kappa_{aq}}$. The on resonance Rabi splitting is given by $\Omega = 2g_{aq} = \frac{1}{2\pi c}\frac{\kappa_{aq}}{\sqrt{\omega_{ant}\omega_{qw}}}$.

l_{ant} (μm)	1.23	1.30	1.38	1.45	1.53	1.60	1.68	1.75	1.83	1.90	1.98
$\tilde{\nu}^0_{ant}$ (cm^{-1})	1843	1704	1585	1482	1391	1311	1239	1175	1117	1064	1016

Table S 1. Fitting parameters for FTIR reflectance measurements

S2.2 Coupled harmonic oscillator model

Considering the non-resonant tip perturbation in our near-field experiments, we consider the Drude response of the tip, with the damping coefficient of 150 cm^{-1} ($\tau_D \sim 30$ fs) determined by the scattering time. We still describe the antenna and quantum well as two oscillators, with the resonance frequencies ω_{ant} and ω_{qw}, and the Lorentzian damping rates γ_{ant} and γ_{qw} . We solve the set of three coupled equations shown in the text to obtain the polarization of the tip using a symbolic equation solver, solving for steady state solutions in the form $x = e^{i\omega t}$. The splitting between the antenna and quantum well in the coupled harmonic oscillator model with a non-resonant tip remains the same as in the two-oscillator model, given by $2g_{aq} = \frac{\kappa_{aq}}{\sqrt{\omega_{ant}}\sqrt{\omega_{qw}}}$. We approximate the IR s-SNOM signal as the induced polarization of the nanotip $P = e \cdot x_{tip}$, which scatters into the far-field proportional to the IR s-SNOM signal.

S2.3 Fit parameters

From fitting the far-field reflectance spectra, we obtain the following parameters: $\tilde{\gamma}^0_{ant}$ = 110 cm^{-1}, $\tilde{\nu}^0_{qw}$ = 1315 cm^{-1}, $\tilde{\gamma}^0_{qw}$ = 110 cm^{-1}, and g_{aq} = 140 cm^{-1}. Additionally, the modeled antenna resonance frequencies $\tilde{\nu}_{ant}$ are proportional to the antenna lengths l_{ant} and are given in Table S.1.

For SINS fitting, we obtain the following parameters: $\tilde{\nu}_{ant}$=1240 cm^{-1}, γ_{ant} =110 cm^{-1}, $\tilde{\nu}_{qw}$=1260 cm^{-1}, and γ_{qw} =110 cm^{-1}. The values for phase delay $\Delta\phi$ and coupling strength g_{aq} at different positions across the antenna are listed in Table S.2.

Table S.3 shows parameters used to model IR s-SNOM with high optical intensity illumination using picosecond laser excitation with parameters $\tilde{\nu}_{ant}$=1240 cm^{-1}, γ_{ant} =110 cm^{-1}, $\tilde{\nu}_{qw}$=1260 cm^{-1}, and γ_{qw} =110 cm^{-1}.

Points	X (μm)	$\Delta\phi$ (rad)	$g_{\rm aq}$ ($\rm cm^{-1}$)
1	0.0	0.2	140
2	0.23	-0.0	140
3	0.46	-0.3	140
4	0.69	-0.5	140
5	0.92	-0.7	140
6	1.15	-0.9	140
7	1.38	-1.1	140
8	1.61	-1.4	140

Table S 2. Model parameters for SINS spectra with low optical illumination intensity.

Points	X (μm)	$\Delta\phi$ (rad)	$g_{\rm aq}$ ($\rm cm^{-1}$)
1	0.18	3.0	73
2	0.30	3.0	68
3	0.53	3.0	58
4	1.07	-0.10	35
5	1.20	-0.10	30
6	1.33	-0.10	24

Table S 3. Model parameters for IR s-SNOM with high optical intensity illumination.

Coupled Maxwell-Bloch model

The parameters of the MQW sample are as follows [1]: the transition frequency between subbands 1 and 2 is, $\tilde{\nu}_{qw} = 1260$ cm^{-1}; the half-linewidth, $\gamma_{qw} = 110$ cm^{-1}, the dipole moment, $d/e = 1.76$ nm; the population decay time, $T_1 = 1.7$ ps; the measured electron density, $\Delta n_0 = 8 \times 10^{17}$ cm^{-3}; the background dielectric constant of the MQW crystal, $\epsilon = 10$. The overlap of the cavity field with the QWs is expected to be significant, given that the MQW stack fills the whole cavity. We take $\Gamma = 0.8$. The cavity resonance frequency and cavity losses could be affected by the tip and its position. The spectra of the antenna field amplitude and phase would be a reliable diagnostics of the antenna-QW detuning; however the spectra of the phase only are

too sensitive to the excitation parameters. We take the cavity frequency and the cavity loss the same as in coupled harmonic oscillator fit, $\tilde{\nu}_{ant} = 1240$ cm^{-1}, close to resonance with the QW, and $\alpha = \gamma_{qw}$, to reproduce the observed linewidth.

S3 ADDITIONAL DATA

S3.1 Spectra under high illumination intensity at different harmonics

We measured and analyzed each of the 1^{st} through 4^{th} harmonic demodulation of the tip scattered signal as we move the s-SNOM tip along the length of an antenna (see Fig. S2 below). As indicated in Fig 1a, for each point 1-9 along the antenna, we show spectra at the (c) 1^{st}, (d) 2^{nd}, and (e) 3^{rd} harmonics under high optical illumination conditions. As expected, the overall signal levels decrease with increasing harmonic, and 4^{th} harmonic demodulated spectra are omitted due to insufficient signal.

In 2^{nd} harmonic (subset of data shown in manuscript) the spectrum (red) from the right end of the antenna is in the weak coupling regime with no discernible peak splitting, whereas with the tip at the left end of the antenna (blue), the system is in strong coupling. In 1^{st} harmonic (c), a similar behavior is observed. Yet because of the admixture of far-field contributions that are dominated by the strongly coupled system, spectrum (9) shows signature of a superposition and interference of weakly coupled near-field and strongly coupled far-field responses. In contrast, in 3^{rd} harmonic a strongly coupled response is observed throughout.

We extend analysis of the influence of tip position on coupling strength to measurements at the 3^{rd} harmonic under high intensity illumination. Experimental spectra at the third harmonic in Fig. S2(e) are shown again in Fig. S3. We compare these experimental spectra with calculated spectra in Fig. S3(b). Calculated spectra match overall experimental trends with two downward peaks when the tip is placed on one end of the antenna (blue spectrum) and two upward peaks shifted in frequency when the tip is placed at the other end of the antenna (red spectrum) Notably however, the calculated splitting coupling strength in Fig. S3(b) varies linearly from g_{aq} = 140 $\mathrm{cm}^{-1}$to g_{aq} = 110 cm^{-1}as a function of tip position despite the high intensity, nearly matching the coupling strength observed under low intensity illumination. We conclude from these measurements that demodulation at a higher harmonic of the tip motion selectively detects a signal that is more strongly coupled and accordingly displays less saturation of the MQW transition.

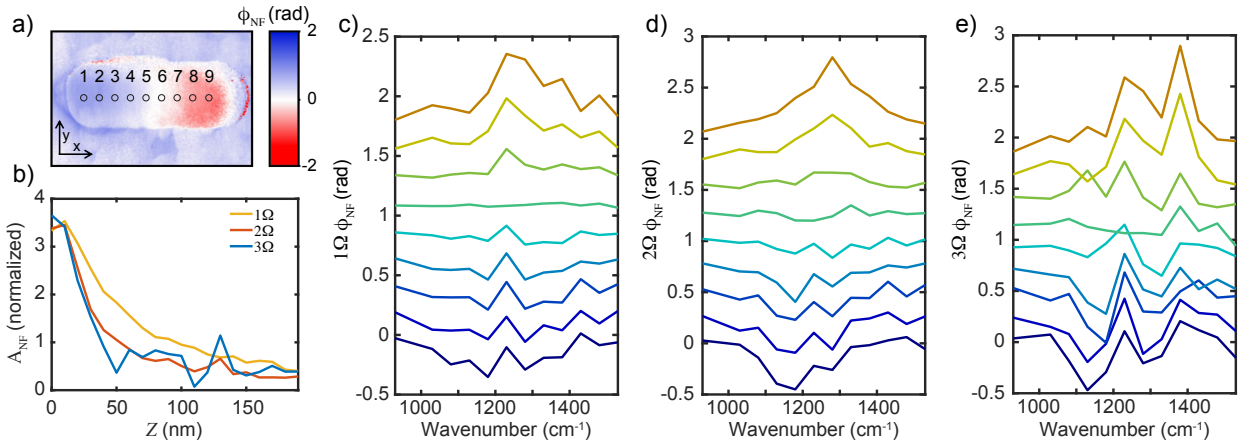

Figure S2. (a) IR s-SNOM phase ϕ_{NF} nano-imaging of a single antenna-MQW heterostructure with tip positions. (b) normalized approach curves on the antenna at $1230\,\mathrm{cm}^{-1}$ at 1^{st} (yellow) to 3^{rd} (blue) harmonics. High illumination intensity IR s-SNOM spectra measured at (c) 1^{st}, (d) 2^{nd} to (e) 3^{rd} harmonics on the antenna at point 1-9 shown in (a).

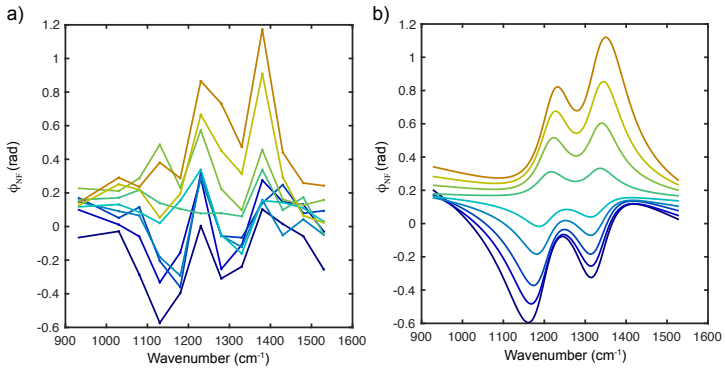

Figure S3. (a) High illumination intensity IR s-SNOM spectra measured at the 3^{rd} harmonic for the line scan shown also shown Fig S2 (e). (b) Corresponding calculated spectra using the coupled oscillator model. The coupling strength is modeled as varying linearly from g_{aq} = 140 $\mathrm{cm}^{-1}$to g_{aq} = 110 cm^{-1}as a function of tip position.

The demodulation-dependent peak splitting associated with antenna-MQW coupling and associated decrease in MQW saturation arises from the different distance-dependence of the near-field signal measured at each harmonic. It is well established that the signal at low harmonics of the tip tapping frequency may still contain contributions from far-field interactions. Signals at higher harmonics reflect increasingly localized fields at the tip apex. We show in (b) the distance-dependent of the tip-scattered signal as the tip approaches the antenna-MQW system, normalized to intensity

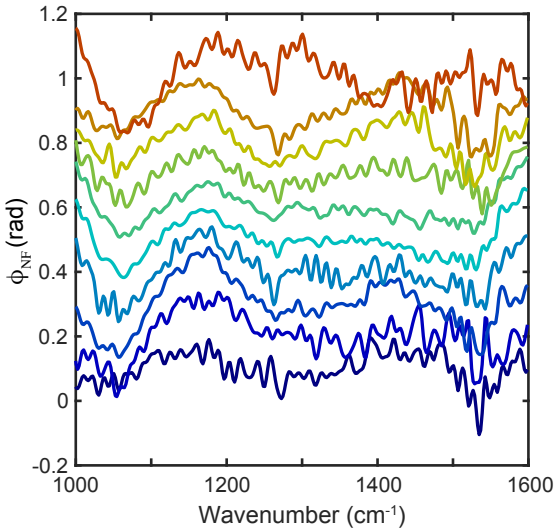

Figure S4. Second-harmonic near-field phase spectra along the antenna, with the antenna-MQW rotated 90°, i.e. perpendicular to incident k-vector.

at closest approach, with the expected approximate exponential distance dependence, and increase in near-field localization with increasing harmonics as established in s-SNOM. In each of the harmonic demodulation, the signal is a superposition of a $local$ tip-sample near-field coupled response (dominated by the QW transition) and $nonlocal$ contributions (dominated by the standing antenna mode). With increasing harmonic demodulation, despite higher field localization and stronger saturation, a corresponding decrease of nano-localized sample volume gives rise to the overall signal being dominated by the delocalized antenna mode, which is dominated by (unsaturated) strong coupling.

S3.2 Strong coupling with the antenna rotated 90°

As control experiment, we rotate the antenna by 90°, i.e., incident k-vector and polarization both perpendicular to the antenna. In this case, as shown in Fig. S4, an overall weak spectral phase and largely flat spectral response is observed as the antenna mode cannot directly be excited by the incident laser field, and only indirectly via the tip-antenna coupling.

S3.3 SINS spectra

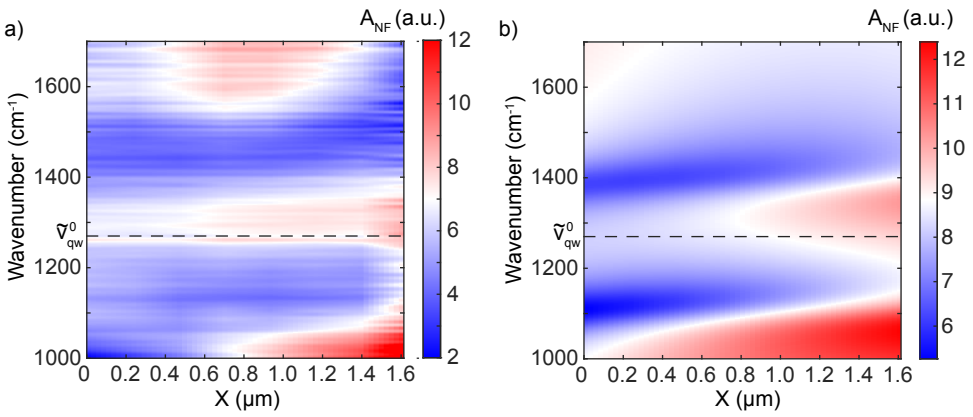

Figure S5. (a) Second harmonic amplitude spectra corresponding to Fig 2c, with the modeled spectra (b) based on coupled oscillator model.

The SINS amplitude spectra corresponding to Fig. 2c are shown in Fig. S5 (a), with coupled oscillator model fitting.

The SINS spectra in Fig. 2 exhibit an apparent spectral shift between antenna and MQW resonance as a function of tip position. This effect, however, is not due to a detuning between antenna and MQW but rather a change in the line shape resulting from the phase difference. In our experiment, we measure the full quadrature of the scattered light. As the phase between driving field of the tip and that of the hybridized antenna-MQW change, the spectrum of the scattered light rotates in the complex plane. Because the peak maximum for an absorptive line shape corresponds to the spectral position of maximum slope for a dispersive (or anti-dispersive) lineshape, apparent detuning is observed as a function of driving phase.

Furthermore, the peaks of the spectral near-field electromagnetic density of states are always red-shifted compared to the far-field emission peaks. This is because coupling to free space is more efficient for shorter wavelength, i.e., higher frequencies. This also causes the collective red shift of MQW transition $\tilde{\nu}_{qw}$ and antenna resonance $\tilde{\nu}_{ant}$ in the near-field as has been described previously [4, 5].

S3.4 Spectra measured when MQW transition is saturated

For comparison, we perform the experiment under saturation condition, with the incidence optical fluence of $\sim 1000\ \mathrm{kW/cm^2}$ [1]. With the MQW transition saturated, in the spectra, only the antenna resonance peaks are visible across the antenna, as shown in Fig. S6a, with corresponding

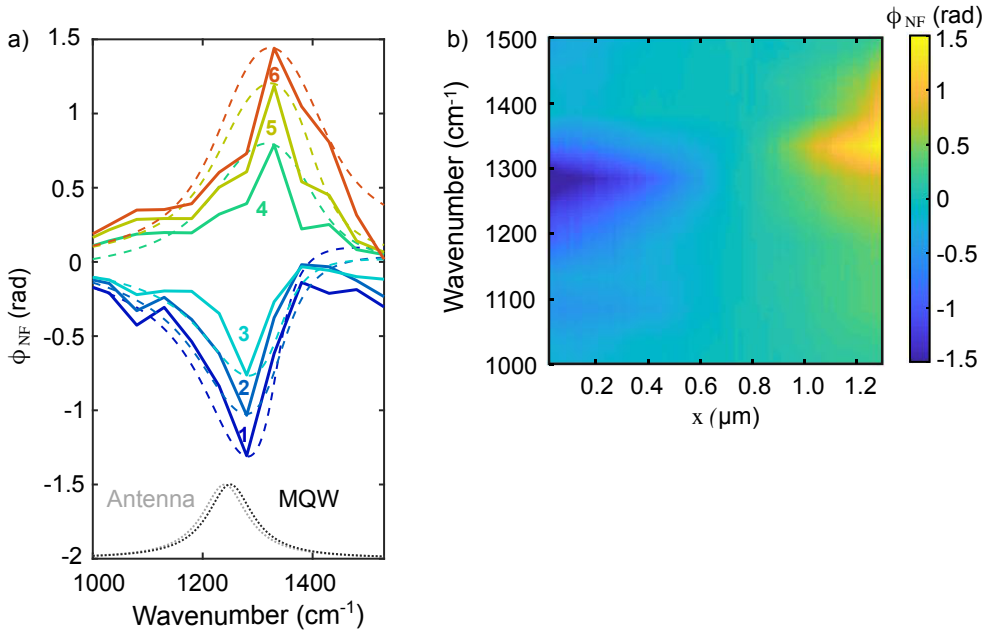

Figure S6. (a) ϕ_{NF} spectra extracted as a function of tip positions across the antenna, with corresponding to the fits of the coupled oscillator model. The dashed grey and black curves show the Lorentzian of fitted antenna and MQW transition resonance. (b) Surface plot of the ϕ_{NF} spectra measured as a function of tip position X along the antenna in steps of 15 nm.

surface plot Fig. S6b. The antenna resonance peaks at one end of the antenna exhibit a red shift of $\sim 50\,\mathrm{cm}^{-1}$, as shown in Fig. S6, which can be explained as the result of phase retardation $\Delta\phi$ changing the excitation pathways of the antenna. We then fit the spectra with the established coupled harmonic oscillator model. The corresponding fits are shown in Fig. S6a (dashed lines), with $\tilde{\nu}_{qw} = 1260\,\mathrm{cm}^{-1}$, $\gamma_{qw} = 100\,\mathrm{cm}^{-1}$, $\tilde{\nu}_{ant} = 1240\,\mathrm{cm}^{-1}$, $\gamma_{ant} = 100\,\mathrm{cm}^{-1}$, and $g_{\mathrm{aq}} = 5\,\mathrm{cm}^{-1}$.

* These authors contributed equally

† emuller@colgate.edu

‡ belyanin@physics.tamu.edu

§ mikhail.belkin@wsi.tum.de

¶ markus.raschke@colorado.edu

[1] Mann, S. A. *et al.* Ultrafast optical switching and power limiting in intersubband polaritonic metasurfaces. *Optica* **8**, 606–613 (2021).

[2] Price, P. Two-dimensional electron transport in semiconductor layers. i. phonon scattering. *Annals of Physics* **133**, 217–239 (1981).

[3] Choe, J.-W., Perera, A., Francombe, M. & Coon, D. Estimates of infrared intersubband emission and its angular dependence in gaas/algaas multiquantum well structures. *Applied Physics Letters* **59**, 54–56 (1991).

[4] Alonso-González, P. *et al.* Experimental verification of the spectral shift between near-and far-field peak intensities of plasmonic infrared nanoantennas. *Physical Review Letters* **110**, 203902 (2013).

[5] Olmon, R. L. *et al.* Determination of electric-field, magnetic-field, and electric-current distributions of infrared optical antennas: a near-field optical vector network analyzer. *Physical Review Letters* **105**, 167403 (2010).